MISSOURI S&T

Missouri University of Science and Technology

Scholars' Mine

Electrical and Computer Engineering Faculty Research & Creative Works

Electrical and Computer Engineering

01 Jan 1995

Remote Detection of Acoustic Boundaries Using Radiation Imaging Operators

Richard E. DuBroff
Missouri University of Science and Technology, red@mst.edu

Md. Ishfaqur Raza

Thomas J. Herrick

Follow this and additional works at: https://scholarsmine.mst.edu/ele_comeng_facwork

Part of the Electrical and Computer Engineering Commons

Remote Detection of Acoustic Boundaries Using Radiation Imaging Operators

Richard E. DuBroff, *Senior Member, IEEE*, M. Ishfaqur Raza, and Thomas J. Herrick

Abstract—In this paper, we present an acoustic imaging operator. This operator is based upon combining the material boundary conditions at an acoustic boundary and the radiation boundary conditions associated with one way wave propagation. Numerical examples, using the second-order imaging operator, are presented in order to demonstrate the applicability of this method to the detection of two-dimensional boundaries.

I. INTRODUCTION

THE USE OF remote measurements to delineate boundaries between acoustically dissimilar materials has applications in many diverse fields. Various approaches have been developed in recent years to produce useful images in areas such as nondestructive evaluation (NDE) and medical diagnostics [1]–[4].

Of particular interest in this study are applications where a significant change is associated with some attribute (such as acoustic impedance) of the system. The present approach consists of constructing a parameter dependent radiation imaging operator (RIO) to remotely detect the boundary between two acoustic media. One of the two media (medium 1) is presumed to be at least partially accessible in the sense that acoustic sources can be appropriately located and that acoustic measurements can be made at some points in medium 1. The other medium is considered to be inaccessible. The acoustic measurements are assumed to consist of recording the values of the total acoustic response (the incident plus scattered acoustic pressure) on some datum surface when the boundary between the two media is insonified by a known acoustic source.

In implementing this approach, the first step is to extrapolate the acoustic pressure measurements ($p_1(r, t)$ evaluated when r is on the datum surface) to yield an estimate of the acoustic pressure throughout medium 1 and to yield an extrapolation of this function into medium 2. The extrapolated pressure will be denoted by $p_e(r, t)$. The problem of wavefield extrapolation (also sometimes referred to as wavefield reconstruction or, in a seismic context, migration) has received extensive attention and there are many well-established methods for accomplishing this task. Some of these methods are based on the Kirchhoff integral [5]–[7]. Other successful methods of extrapolation have been based on a frequency domain representation of the acoustic wave equation [8], [9]. The type of extrapolation used here is based on the finite difference time
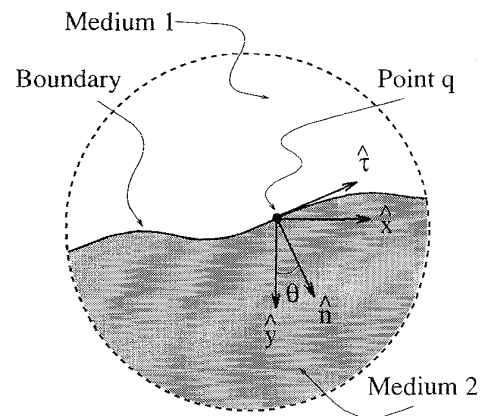
Fig. 1. A small portion of the boundary between two acoustic materials.

domain implementation of the acoustic wave equation and is based on earlier work by Claerbout [10], [11] and McMechan [12].

Because the methods of wavefield extrapolation are well documented, the next section begins by describing the construction of a second-order radiation imaging operator (RIO) starting from the conditions satisfied by the pressure at the boundary between the two media. The RIO is based on combining material boundary conditions with radiation boundary conditions (RBC's). The RBC's proposed by Engquist and Majda [13], [14], as well as those proposed by Bayliss and Turkel [15], have been implemented in various forms and applied to a wide range of problems in wave propagation [16]–[18]. The present approach to developing the RIO is based upon the RBC's proposed by Engquist and Majda [13], [14]. The second-order RIO is then applied to the extrapolated pressure. The output of the operator, when suitably processed, is shown to yield an image of the boundary between the two materials.

The results cited in this account were all based upon the numerical simulation of acoustic measurements. The procedures used to obtain the simulated measurements are described in Section III and the results of applying the RIO are found in Section IV.

II. A SECOND-ORDER RADIATION IMAGING OPERATOR

Fig. 1 shows a small portion of a boundary between two acoustic media with point q denoting one point on the boundary.

Using $p_1(\mathbf{r}, t)$ and $p_2(\mathbf{r}, t)$ to represent the acoustic pressure in these media, the material boundary conditions (MBC's) impose continuity of the pressure and its normal derivative at each point q

$$p_1(\mathbf{r}, t)|_q = p_2(\mathbf{r}, t)|_q \quad (1)$$

and

$$\frac{\partial}{\partial n} p_1(\mathbf{r}, t)\bigg|_q = \frac{\partial}{\partial n} p_2(\mathbf{r}, t)\bigg|_q \quad (2)$$

provided the mass densities of the two media are equal.

Letting s represent a continuously varying parameter (e.g., arc length) along the curve describing the boundary and differentiating (1) along the boundary

$$\frac{d^k}{ds^k} p_1(\mathbf{r}, t)|_q = \frac{d^k}{ds^k} p_2(\mathbf{r}, t)|_q \quad (3)$$

for derivatives of order k. When $k = 1$, (3) is equivalent to requiring continuity of the tangential derivative of pressure at point q. Thus, the MBC's in the case of equal mass densities ($\rho_1 = \rho_2$) imply continuity of all first-order spatial derivatives [20]. In addition, both MBC's may be differentiated with respect to time to show that

$$\frac{\partial^m}{\partial t^m} p_1(\mathbf{r}, t)\bigg|_q = \frac{\partial^m}{\partial t^m} p_2(\mathbf{r}, t)\bigg|_q \quad (4)$$

and

$$\frac{\partial^{m+1}}{\partial n \partial t^m} p_1(\mathbf{r}, t)\bigg|_q = \frac{\partial^{m+1}}{\partial n \partial t^m} p_2(\mathbf{r}, t)\bigg|_q \quad (5)$$

for m-th order partial differentiation with respect to time. Although the assumption of equal mass densities may seem unduly restrictive, it will be shown, in subsequent numerical examples, that the RIO can tolerate some degree of uncertainty in the values of its parameters. These numerical results suggest that the RIO presented here may be able to tolerate small density contrasts. Large density contrasts would require modifying (2) and would also require a somewhat modified approach in the numerical procedure for obtaining simulated data (described in Section III).

In developing second-order RIO's, it is sufficient for the pressures, $p_1(\mathbf{r}, t)$ and $p_2(\mathbf{r}, t)$ to be differentiable to the second order. Higher order RIO's (which will not be considered here) impose correspondingly more stringent differentiability requirements of these pressures.

To the extent that $p_2(\mathbf{r}, t)|_q$ represents a wave radiating away from the boundary, $p_2(\mathbf{r}, t)|_q$ can be regarded as a solution of the one way wave equation

$$\mathcal{L}^+ p_2(\mathbf{r}, t)\big|_q = \left\{ \frac{\partial}{\partial n} + \frac{1}{c_2} \frac{\partial}{\partial t} \sqrt{1 - c_2^2 \frac{\partial_{\tau\tau}^2}{\partial_{tt}^2}} \right\} p_2(\mathbf{r}, t)\big|_q = 0 \quad (6)$$

and by approximating the pseudodifferential operator $\mathcal{L}^+$ with a two-term Taylor series expansion [18]

$$\left\{ c_2 \partial_{nt}^2 + \partial_{tt}^2 - (1/2) c_2^2 \partial_{\tau\tau}^2 \right\} p_2(\mathbf{r}, t)|_q = 0 \quad (7)$$

can be regarded as a second-order RBC satisfied by the pressure in medium 2 at each point on the boundary. It should

again be emphasized that the two media are presumed to be homogeneous. A more general approach would be required if the media were inhomogeneous [19].

All of the terms in this equation involve second-order differentiation. Furthermore, the derivatives appearing in the first two terms are continuous at the boundary. Consequently, the second-order RBC may be partially rewritten in terms of $p_1(\mathbf{r}, t)$ as

$$\left\{ c_2 \partial_{nt}^2 + \partial_{tt}^2 \right\} p_1(\mathbf{r}, t)|_q - (1/2) c_2^2 \partial_{\tau\tau}^2 p_2(\mathbf{r}, t)|_q = 0. \quad (8)$$

The differentiation of $p_1(\mathbf{r}, t)$ is more convenient (from a numerical point of view) if the differentiation is performed with respect to the global variables x, y, and t. Thus, the first two terms in (8) can be replaced with

$$\left\{ c_2 \partial_{nt}^2 + \partial_{tt}^2 \right\} p_1(\mathbf{r}, t)|_q =$$
$$\left\{ c_2 \left[n_x \partial_{xt}^2 + n_y \partial_{yt}^2 \right] + \partial_{tt}^2 \right\} p_1(\mathbf{r}, t)|_q \quad (9)$$

where n_x and n_y are the x and y components of the unit vector $\hat{n}$ at point q (see Fig. 1).

To write the third term in (8) in terms of $p_1(\mathbf{r}, t)|_q$, the second-order tangential derivative may first be expressed in terms of the global variables as

$$\partial_{\tau\tau}^2 p_2(\mathbf{r}, t)|_q = [n_y \partial_x - n_x \partial_y]^2 p_2(\mathbf{r}, t)|_q$$
$$= \left\{ n_y^2 \partial_{xx}^2 - 2 n_x n_y \partial_{xy}^2 + n_x^2 \partial_{yy}^2 \right\} p_2(\mathbf{r}, t)|_q. \quad (10)$$

The continuity of the second-order arc length derivative ((3) with $k = 2$) may also be expressed in terms of global variables to show that

$$\left\{ x'' \partial_x + y'' \partial_y + (x')^2 \partial_{xx}^2 + 2x'y' \partial_{xy}^2 + (y')^2 \partial_{yy}^2 \right\} p_2(\mathbf{r}, t)|_q =$$
$$\left\{ x'' \partial_x + y'' \partial_y + (x')^2 \partial_{xx}^2 + 2x'y' \partial_{xy}^2 + (y')^2 \partial_{yy}^2 \right\} p_1(\mathbf{r}, t)|_q \quad (11)$$

with primes indicating arc length derivatives of x and y along the boundary. Since the first-order spatial derivatives of $p_1(\mathbf{r}, t)$ and $p_2(\mathbf{r}, t)$ are equal at each point q on the boundary, this equation may be reduced to

$$\left\{ (x')^2 \partial_{xx}^2 + 2x'y' \partial_{xy}^2 + (y')^2 \partial_{yy}^2 \right\} p_2(\mathbf{r}, t)\big|_q =$$
$$\left\{ (x')^2 \partial_{xx}^2 + 2x'y' \partial_{xy}^2 + (y')^2 \partial_{yy}^2 \right\} p_1(\mathbf{r}, t)\big|_q. \quad (12)$$

The arc length derivatives of the x and y coordinates along the boundary may, in turn, be written in terms of the components of the boundary normal vector $\hat{n}$ by noting

$$x' = \tau_x = n_y$$
$$y' = \tau_y = -n_x$$

in which case (12) becomes

$$\left\{ n_y^2 \partial_{xx}^2 - 2 n_x n_y \partial_{xy}^2 + n_x^2 \partial_{yy}^2 \right\} p_2(\mathbf{r}, t)|_q =$$
$$\left\{ n_y^2 \partial_{xx}^2 - 2 n_x n_y \partial_{xy}^2 + n_x^2 \partial_{yy}^2 \right\} p_1(\mathbf{r}, t)|_q. \quad (13)$$

Comparing the left side of the present equation with the right side of (10) allows the second-order tangential derivative of
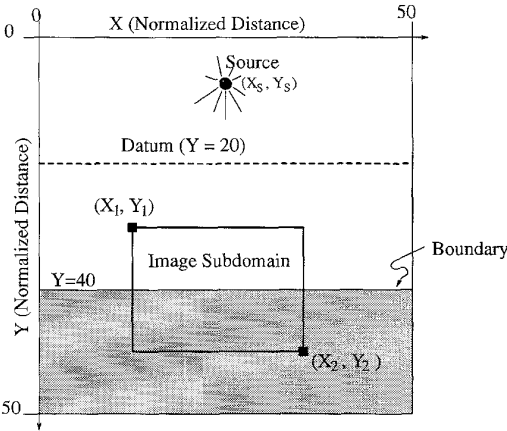
Fig. 2. Simulation geometry for a flat boundary.

$p_2(\mathbf{r}, t)$ at each point on the boundary to be computed from a knowledge of the second-order partial derivatives of $p_1(\mathbf{r}, t)$ in accordance with

$$\partial^2_{\tau\tau} p_2(\mathbf{r}, t)\big|_q = \left\{ n_y^2 \partial^2_{xx} - 2n_x n_y \partial^2_{xy} + n_x^2 \partial^2_{yy} \right\} p_1(\mathbf{r}, t)\big|_q. \tag{14}$$

Finally, substituting (14) and (9) into (8) gives

$$\left\{ c_2 \left[n_x \partial^2_{xt} + n_y \partial^2_{yt} \right] + \partial^2_{tt} \right.$$

$$\left. - (1/2)c_2^2 \left[n_y^2 \partial^2_{xx} - 2n_x n_y \partial^2_{xy} + n_x^2 \partial^2_{yy} \right] \right\} p_1(\mathbf{r}, t)\big|_q = 0. \tag{15}$$

The specific combination of parameters (n_x, n_y, and c_2) and partial differential operators, appearing within the braces on the left side of this equation, provides an example of a second-order radiation imaging operator (RIO). This linear operator will be denoted symbolically by $\mathcal{L}_{rio}(n_x, n_y, c_2)$. Once the parameters of the operator have been selected, the operator $\mathcal{L}_{rio}$ can be applied to $p_1(\mathbf{r}, t)$ to produce an output in the form of a function of time and position. Equation (15) states that when this operator is applied to $p_1(\mathbf{r}, t)$ and is subsequently evaluated at a point on the boundary (point q), the output is zero. In practice, the right side of (15) will not be exactly zero at a point on the boundary due to the approximations inherent in the RBC's.

III. NUMERICAL PROCEDURE

To demonstrate the application of this RIO, three different geometric boundaries between the upper and lower half spaces shown in Fig. 2 were considered.

In the first case, the boundary between the two half spaces consisted of a flat horizontal surface (as shown in Fig. 2). In the second case, the boundary consisted of a notched horizontal surface (Fig. 3(a)), while in the third case part of the boundary consisted of a horizontal segment combined with an inclined segment as shown in Fig. 3(b).

The first step in each of the three cases consisted of using the finite difference time domain approach to simulate the process of acquiring a sampled set of data on the surface labeled "datum" in Fig. 2. Velocities c_1 and c_2 where chosen to be

1000 and 1500 m/s, respectively, while the mass densities ρ_1 and ρ_2 were chosen to be equal. Computational mesh points occurring on the boundary between the two half spaces were assigned a velocity equal to the average of c_1 and c_2, as suggested in a paper by Zhang and Mei [21].

The spatial and temporal sampling intervals used in the finite difference simulations were $\delta_x = \delta_y = 50$ m and $\delta_t = 0.0167$ s. The normalized coordinates and normalized time, as indicated with capital letters, refer to distances in meters divided by δ_x and time in seconds divided by δ_t. For the velocities used in these simulations, the spatial and temporal sampling intervals were consistent with the Courant stability criteria [22].

In all cases, the datum consisted of a horizontal surface located at a normalized depth of $Y = 20$ and the source signature consisted of a Gaussian pulse [21]

$$s(T) = A \exp\left\{ -\left[\frac{T - 10}{20} \right]^2 \right\}. \tag{16}$$

Using the 40-dB bandwidth points of the source's power spectrum to establish a nominal upper limit on the frequency of the source, the computational domain shown in Fig. 2 is roughly eight wavelengths long on each edge. The major portion of the source's power spectrum falls into a region over which the spatial sampling interval comprises one-tenth or less of the wavelength in order to reduce the effects of numerical dispersion [22].

With the exception of the results to be presented in Fig. 6, the normalized source coordinates were $X_s = 25$ and $Y_s = 15$. The discretized version of the acoustic wave equation is

$$p(X, Y, T) = 2p(X, Y, T - 1) - p(X, Y, T - 2)$$
$$+ s(T)f(X, Y) + \frac{c^2(\delta_t)^2}{(\delta_x)^2}$$
$$\cdot \{ p(X + 1, Y, T - 1) - 4p(X, Y, T - 1)$$
$$+ p(X - 1, Y, T - 1) + p(X, Y + 1, T - 1)$$
$$+ p(X, Y - 1, T - 1) \} \tag{17}$$

where $f(X, Y)$ is one when $X = X_s$ and $Y = Y_s$ and zero everywhere else. Discretized second-order RBC's [16], [23] were used to terminate the computational domain on the surfaces defined by $X = 0$, $X = 50$, $Y = 0$, and $Y = 50$. For example, the second-order RBC applied at $X = 0$ in discretized form is

$$p(0, Y, T) = -p(1, Y, T - 2)$$
$$+ \frac{c\delta_t - \delta_x}{c\delta_t + \delta_x} \{ p(1, Y, T) + p(0, Y, T - 2) \}$$
$$+ \frac{2.0\delta_x}{c\delta_t + \delta_x} \{ p(0, Y, T - 1) + p(1, Y, T - 1) \}$$
$$+ \frac{c^2\delta_t^2}{2\delta_x(c\delta_t + \delta_x)} \{ p(0, Y + 1, T - 1)$$
$$- 2.0p(0, Y, T - 1) + p(0, Y - 1, T - 1) \}$$
$$+ \frac{c^2\delta_t^2}{2\delta_x(c\delta_t + \delta_x)} \{ p(1, Y + 1, T - 1)$$
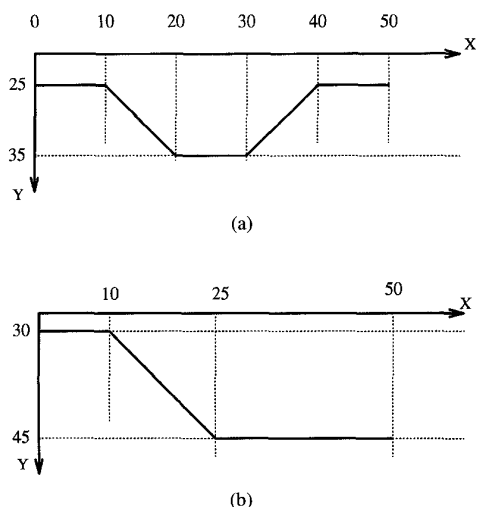$$- 2.0p(1, Y, T - 1) + p(1, Y - 1, T - 1) \}. \tag{18}$$

Fig. 3. Additional boundaries between the two half spaces shown in Fig. 2. (a) Notched boundary. (b) Asymmetric boundary.

In each case, the simulation was run twice with 401 time samples ($0 \leq T \leq 400$) per run. The first run of the simulation was used to obtain the incident wave contribution to the sampled values of $p(X, Y, T)$ on the datum ($Y = 20$). In this first run, the value of c_2 was set equal to the value of c_1 (1000 m/s). In the second run, the value of c_2 was set equal to 1500 m/s. The sampled values of $p(X, Y, T)|_{Y=20}$ in the second run then contained contributions from both the incident and scattered waves. By comparing the sampled values from these two runs it was possible to separate the individual contributions of the incident and scattered waves. The sampled values of the incident and scattered waves on the datum were used in the second step of the process, namely wavefield extrapolation.

The purpose of the wavefield extrapolation is to calculate the total wavefield, $p_e(\mathbf{r}, t)$, at all points below the datum, assuming that the wavefield propagates with a velocity of c_1. Ideally, the extrapolated wavefield should agree with the simulated wavefield at all times and at all points between the datum and the boundary. Below the boundary, the extrapolated wavefield should be regarded as a mathematical extension of the wavefield existing above the boundary [20]. The incident wave contribution to $p(X, Y, T)|_{Y=20}$ was extrapolated using the FD-TD approach in forward time while the scattered portion of $p(X, Y, T)|_{Y=20}$ was extrapolated using the FD-TD approach in backward time [12]. The initial conditions (prior to $T = 0$) for the forward time FD-TD extrapolation consisted of assuming that the pressure was identically zero. The final conditions (after $T = 401$) for the backward time FD-TD extrapolation consisted of assuming that the pressure was also identically zero, even though the pressure obtained in the simulation had not yet reached this terminal value at $T = 401$ samples.

IV. NUMERICAL RESULTS

In all three cases, the assumed values for the final conditions would be expected to introduce some error in the extrapola-
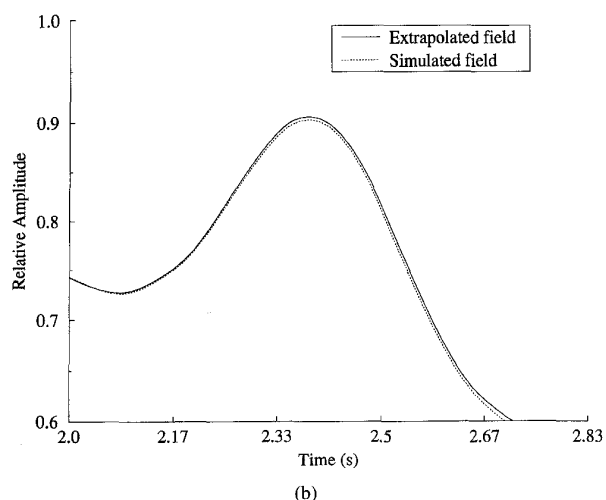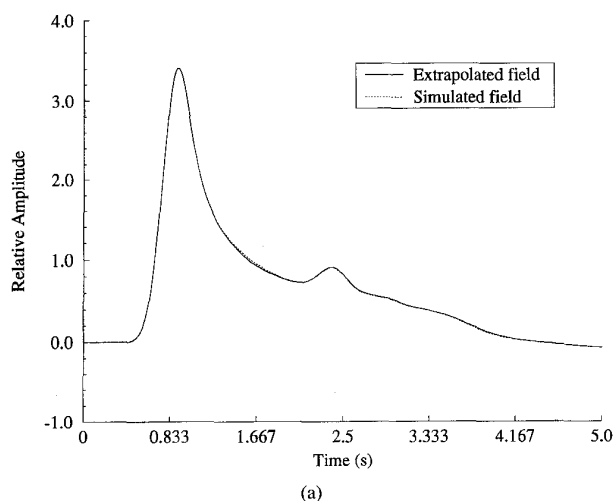

Fig. 4. A comparison of the simulated and extrapolated records of pressure at $(X, Y) = (25, 25)$: (a) for the entire record length, and (b) for a selected portion of the record length containing the reflected pulse.

tion process. In the simplest case (the horizontal reflector), this error is indicated by the small discrepancy between the simulated and extrapolated waves shown in Fig. 4.

The time functions shown in this figure were obtained at the single spatial point $X = 25, Y = 25$. Fig. 4(a) indicates the magnitude of the discrepancy over the entire record length, while Fig. 4(b) shows the discrepancy over a time interval corresponding to the arrival of the reflected pulse. A point by point comparison of the terminal pressure values with the peak pressure values suggests that the absolute value of the terminal pressure is less than 5% of the absolute value of the peak pressure at each spatial sample point considered. Allowing a longer record length ($T > 401$) results in an even smaller error. Letting $T = 1000$, for example, was found to reduce the absolute value of this ratio (terminal to peak pressure) to less than 2%.

Nevertheless, the RIO given in (15) was applied to the extrapolated wavefield ($p_e(\mathbf{r}, t)$) using the parameters $c_2 =$
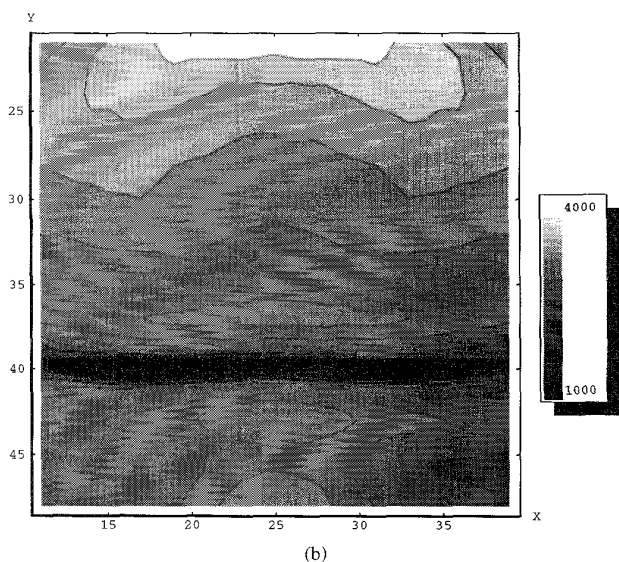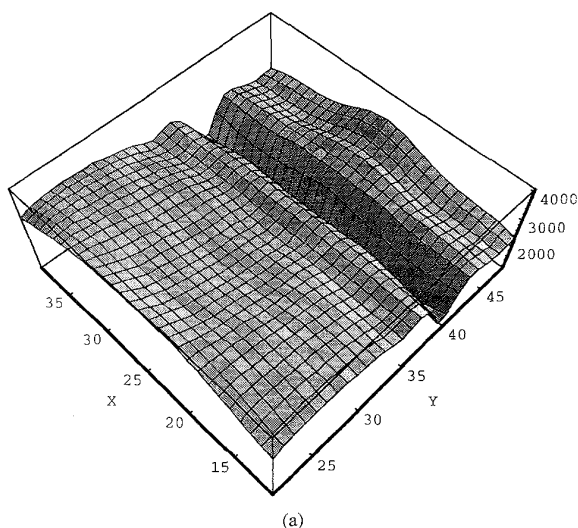
(a)

(b)

Fig. 5.   Image surface for a flat boundary: (a) 3-D view, and (b) contour view.

Fig. 6.   An example of the effect of changing the source to boundary separation distance.

1500 m/s, $n_x = 0$, and $n_y = 1$. The average absolute value of the output of this operator, denoted here by

$$\langle |\mathcal{L}_{rio}(n_x, n_y, c_2)p_e(\mathbf{r}, t)| \rangle_t$$

was calculated at each point in the image subdomain ($[X_1, X_2] \times [Y_1, Y_2] = [11, 39] \times [21, 49]$) to produce an image of the boundary, and the results are presented in the form of a 3-D image surface (Fig. 5(a)) and a gray scale plot (Fig. 5(b)). The location of the boundary is indicated by a minimum in the value of $\langle |\mathcal{L}_{rio}p_e(\mathbf{r}, t)| \rangle_t$.

The image subdomain used in all of the examples is a subset of the computational domain. The size of this subdomain is dictated by storage limitations in the plotting software used.

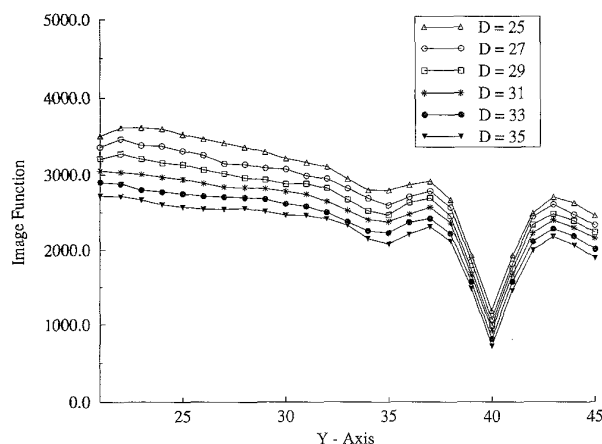Fig. 6 shows one vertical slice (along $X = 25$) through an image surface for several different normalized source to

boundary separations in the range of $D = 25$ to $D = 35$ where D is the shortest distance between the source and the boundary, i.e.,

$$D = 40 - Y_s.$$

The source to boundary distance was changed by moving the source within the computational domain of Fig. 2, while keeping the datum and boundary locations fixed. In all cases, the minimum occurs at the same point $Y = 40$, but the minimum is generally lower as the source to boundary distance increases. This result can be interpreted in terms of the increased accuracy of the second-order RBC (and hence of the second-order RIO) in the far field. However, as the source to boundary distance increases by moving the source upward (away from the boundary), the RBC at $Y = 0$ (used in simulating the sampled wavefield on the datum) is less accurate. Thus, the increased accuracy of the RIO in this simulation is partially offset by the decreasing accuracy of the wavefield on the datum.

With the source to boundary distance maintained at $D = 25$, the next figure (Fig. 7) shows the effect of using incorrect values for the parameter c_2 in the second-order RIO. Again, this figure consists of a vertical slice ($X = 25$) through the image surface for a range of different choices for c_2. Generally, when c_2 is close to the correct value, the minimum occurs near $Y = 40$; but, as c_2 departs significantly from the correct value, the minimum at $Y = 40$ disappears.

Fig. 8 shows, in a similar manner, the dependence of the image upon misalignment of the boundary normal direction. The correct values of parameters n_x and n_y are 0 and 1. For misaligned boundary normal directions, n_x and n_y can be written as

$$n_x = \sin(\theta)$$
$$n_y = \cos(\theta)$$

where θ is defined in Fig. 1. The effect of this misalignment is shown for several values of θ between 0 and 45°. Given the symmetry of Fig. 2 about $X = 25$, the effect of angular misalignment for a negative value of θ would be expected to be identical to the effect for the corresponding positive angle.
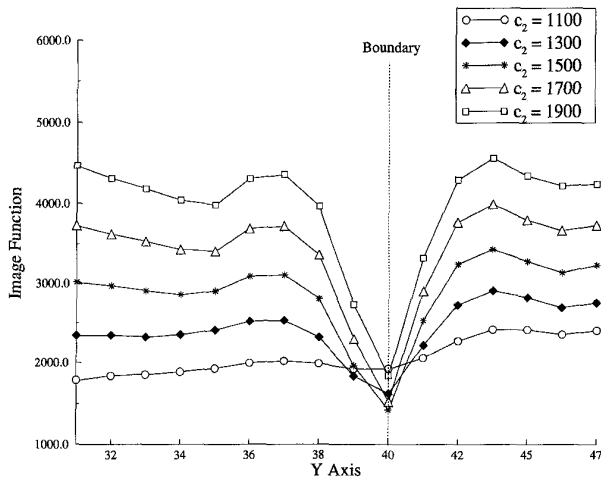
Fig. 7. An example of the effect of an incorrect selection for parameter c_2.
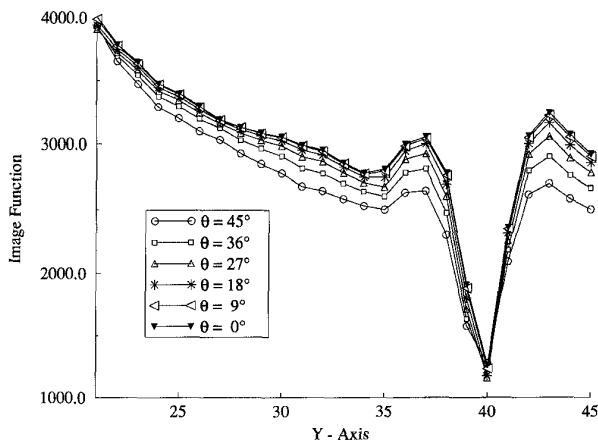

Fig. 8. An example of the effect of misalignment in the boundary normal direction.

Figs. 9 and 10 show the 3-D and gray scale representations of the image surfaces for the notched and asymmetric boundaries. In these cases, the RIO used $n_x = 0$, $n_y = 1$, and $c_2 = 1500$ throughout the image subdomain.

V. CONCLUSIONS

The combination of material boundary conditions (MBC's) with a second-order radiation boundary condition (RBC) has been shown to provide the basis for constructing a radiation imaging operator (RIO). Several numerical examples have been considered to show how the RIO can be used to detect the geometric configuration of an acoustic boundary.

In theory, it should be possible to develop higher order RBC's although an extension of this type would be expected to yield operators containing a larger number of parameters. Also, all of the examples considered to this point have consisted of boundaries between two acoustic half spaces. Thus, the effect of multiple reflections in the second material has not, as yet, been addressed.

The MBC's, as expressed by (1) and (2), would seem to limit the applicability of this proposed method to acoustic
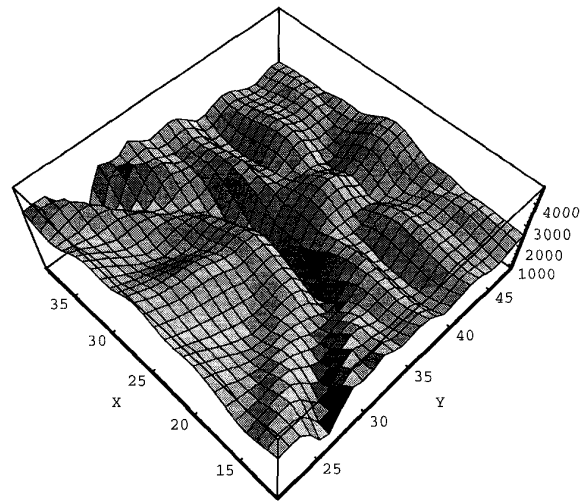
(a)
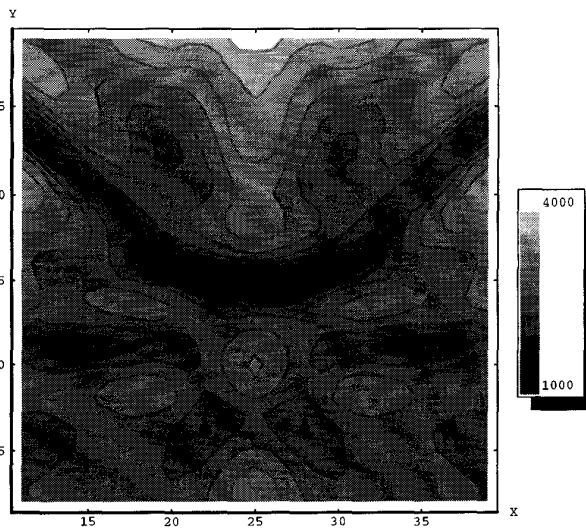
(b)

Fig. 9. Image surface for a notched boundary: (a) 3-D view, and (b) contour view.

materials having equal mass densities. In practice, this condition is unlikely to be satisfied. Nonetheless, for small density contrasts, the ability of this method to tolerate small errors in velocity suggests that the method might also be able to tolerate small errors caused by assuming equal mass densities. For larger density contrasts (where the discontinuity in the pressure gradient cannot be ignored) and/or materials capable of supporting shear waves, the MBC's used here would be inapplicable. By choosing a different set of MBC's it may be possible to extend this method to include materials having different densities and/or materials capable of supporting shear waves. In any case, the resulting RIO's would likely be more complicated and would also be expected to depend on additional parameters.

While the performance of the RIO considered here certainly depends upon the accuracy of the parameters (n_x, n_y, and
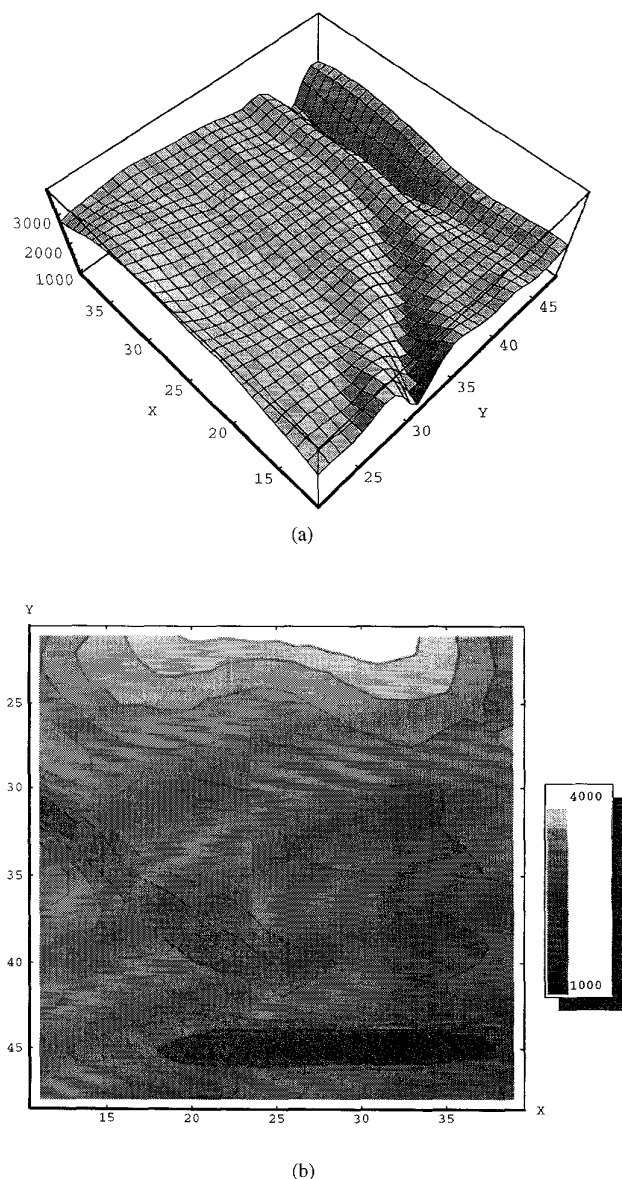
(a)

(b)

Fig. 10. Image surface for an asymmetric boundary: (a) 3-D view, and (b) contour view.

c_2), the numerical examples considered suggest that the RIO can, in many cases, tolerate some degree of uncertainty in the parameter values.

ACKNOWLEDGMENT

REFERENCES

[1] R. A. Kline, Y. Q. Wang, R. B. Mignigna, and P. O. Delsanto, "A finite-difference approach to acoustic tomography in anisotropic media," *J. Nondestructive Evaluation*, vol. 13, no. 2, pp. 75–83, 1994.

[2] H. Ermert and R. Karg, "Multifrequency acoustical holography," *IEEE Trans. Son. Ultrason.*, vol. SU-26, pp. 279–286, July 1979.

[3] S. J. Wernecke and L. R. D'Addario, "Maximum entropy image reconstruction," *IEEE Trans. Comput.*, vol. C-26, pp. 351–364, Apr. 1977.

[4] J. T. Tlitalo and H. Ermert, "Ultrasound synthetic aperture imaging: Monostatic approach," *IEEE Trans. Ultrason., Ferroelec., Freq. Contr.*, vol. 41, pp. 333–339, May 1994.

[5] C. P. A. Wapenaar, G. L. Peels, V. Budejicky, and A. J. Berkhout, "Inverse extrapolation of primary seismic waves," *Geophysics*, vol. 54, pp. 853–863, July 1989.

[6] W. A. Schneider, "Integral formulation for migration in two and three dimensions," *Geophysics*, vol. 43, pp. 49–76, 1978.

[7] J. W. Goodman, *Introduction to Fourier Optics*. San Fransisco: McGraw-Hill, 1968.

[8] R. H. Stolt, "Migration by Fourier transform," *Geophysics*, vol. 43, pp. 23–48, Feb. 1978.

[9] J. Gazdag, "Wave equation migration with the phase-shift method," *Geophysics*, vol. 43, pp. 1342–1351, 1978.

[10] J. F. Claerbout and S. M. Doherty, "Downward continuation of moveout corrected seismograms," *Geophysics*, vol. 37, pp. 741–768, Oct. 1972.

[11] J. F. Claerbout, *Fundamentals of Geophysical Data Processing*. New York: McGraw-Hill, 1976.

[12] W. F. Chang and G. A. McMechan, "3D acoustic reverse-time migration," *Geophysical Prospecting*, vol. 37, pp. 243–256, Apr. 1989.

[13] B. Engquist and A. Majda, "Absorbing boundary conditions for the numerical simulation of waves," *Math. Comput.*, vol. 31, pp. 629–651, July 1977.

[14] ———, "Radiation boundary conditions for acoustic and elastic wave calculations," *Commun. Pure Applied Math.*, vol. 32, pp. 313–357, 1979.

[15] A. Bayliss and E. Turkel, "Radiation boundary conditions for wave-like equations," *Commun. Pure Applied Math.*, vol. 33, pp. 707–725, 1980.

[16] G. Mur, "Absorbing boundary conditions for the finite-difference approximation of the time-domain electromagnetic-field equations," *IEEE Trans. Electromagn. Compat.*, vol. EMC-23, pp. 377–382, Nov. 1981.

[17] G. A. Kriegsmann, A. Taflove, and K. R. Umashankar, "A new formulation of electromagnetic wave scattering using an on-surface radiation boundary condition approach," *IEEE Trans. Antenn. Propagat.*, vol. AP-35, pp. 152–161, Feb. 1987.

[18] T. G. Moore, J. G. Blaschak, A. Taflove, and G. A. Kriegsmann, "Theory and application of radiation boundary operators," *IEEE Trans. Antenn. Propagat.*, vol. AP-36, pp. 1797–1812, Dec. 1988.

[19] L. Fishman, "Exact and operator rational approximate solutions of the Helmholtz, Weyl composition equation in underwater acoustic—The quadratic profile," *J. Math. Phys.*, vol. 33, no. 5, pp. 1887–1914, May 1992.

[20] R. E. DuBroff, "Acoustic imaging and the juxtaposition of waves," *J. Geophysical Res.*, vol. 91, pp. 3784–3794, Mar. 1986.

[21] X. Zhang and K. K. Mei, "Time-domain finite difference approach to the calculation of the frequency-dependent characteristics of microstrip discontinuities," *IEEE Trans. Microwave Theory Tech.*, vol. MTT-36, pp. 1775–1787, Dec. 1988.

[22] W. C. Chew, *Waves and Fields in Inhomogeneous Media*. New York: Van Nostrand Reinhold, 1990.

[23] M. I. Raza, "Finite-difference time-domain analysis in two-dimensions," M.S. thesis, Univ. of Missouri-Rolla, 1993.
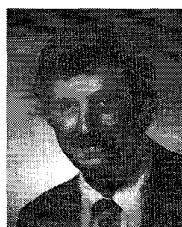
Richard E. DuBroff (S'74–M'74–M'77–SM'84) received the B.S.E.E. degree from Rensselaer Polytechnic Institute, Troy, NY, in 1970, the M.S. degree from the University of Illinois-Urbana in 1972, and the Ph.D. degree from the University of Illinois in 1976. His dissertation concerned atmospheric acoustic gravity waves.

From 1976 to 1978, he held a postdoctoral position in the Ionosphere Radio Lab and worked on backscatter inversion of ionospheric electron density profiles. From 1978 to 1984, he was employed as a Research Engineer in the geophysics branch of Phillips Petroleum (Bartlesville, OK). Since 1984, he has been affiliated with the University of Missouri-Rolla where he is currently an Associate Professor of Electrical Engineering. His research interests include electromagnetics, geophysics, and signal processing as applied to nondestructive evaluation and remote sensing.

Dr. DuBroff is a registered Professional Engineer.

M. Ishfaqur Raza was born in Dhaka, Bangladesh in 1966. He received the B.S. degree from Bangladesh University of Engineering and Technology, Dhaka, in 1991, and the M.S. degree from the University of Missouri-Rolla, Rolla, in 1994, both in electrical engineering. He is currently pursuing the Ph.D. degree at the University of Missouri-Rolla, where he has been a Research and Teaching Assistant.

His research interests include electromagnetics, nondestructive evaluation, and the FD-TD method applied to electromagnetic and acoustic wave propagation.

Thomas J. Herrick received the B.S.E.E. degree from the University of Missouri-Rolla in 1957. He received the M.S.E.E. degree from the University of Missouri-Rolla in 1963.

He was employed at the Naval Weapons Center, China Lake, CA, from 1957 to 1961. Currently, he is an Associate Professor in the Department of Electrical Engineering at the University of Missouri-Rolla, and also serves as the Coordinator for Industrial Grants and Contracts for the Intelligent Systems Center. His research interests include acoustics and signal processing for biomedical and manufacturing applications.